Journal of Fluids and Structures 91 (2019) 102706

Contents lists available at ScienceDirect

Journal of Fluids and Structures

journal homepage: www.elsevier.com/locate/jfs

On the mechanism of symmetric vortex shedding

Krishnan Hrisheekesh [a], Amit Agrawal [b,*], Atul Sharma [b], Mark C. Thompson [c], John Sheridan [c]

[a] Research Scholar, IITB-Monash Research Academy, India
[b] Department of Mechanical Engineering, Indian Institute of Technology Bombay, Powai, Mumbai 400076, India
[c] Fluids Laboratory for Aeronautical and Industrial Research (FLAIR), Department of Mechanical and Aerospace Engineering, PO Box 31, Monash University, 3800, Clayton, Australia

ARTICLE INFO

Article history:
Received 24 October 2018
Received in revised form 8 June 2019
Accepted 9 August 2019
Available online xxxx

ABSTRACT

In this paper, we study the vortex-shedding mechanism of a square cylinder subjected to a mean flow with a superimposed pulsatile flow, under symmetric vortex shedding conditions. The near-body vortical events are interpreted in accordance with the two-dimensional vorticity transport equation, and the interactions between different vortical regions are quantified by circulation balance for a control volume in the near wake. Strong wake counter flow that splits into two branches, with one branch considerably disrupting the boundary layer while other branch cuts off supply of vorticity to the shear layer, is found to be an essential feature of symmetric vortex shedding. To further clarify the roles of correlated terms contributing to the vorticity generation and transport in the wake, the Reynolds number was varied while keeping other excitation parameters constant. This results in the intensity of symmetric vortex shedding increasing with Reynolds number. The increase in wake counter-flow strength with increased Reynolds number cannot be explained either by a relative velocity between the mean and pulsatile flow components or relative acceleration between bluff body and fluid. Based on the results it is inferred that the brief rolling up of the shear layer to form a wake vortex during a part of the pulsation cycle, together with the associated unsteady tangential pressure gradient around the body, contribute to the stronger wake counter flow at higher Reynolds numbers. At lower pulsation amplitudes, the tendency of the fluid in the wake to form strong counter flow can interact significantly with the transverse entrainment flow to alter the natural vortex-shedding mechanism, to give different vortex-shedding modes.

1. Introduction and literature survey

The natural vortex-shedding mechanism of bluff bodies can be significantly altered by various forms of excitation, such as bluff-body motion, nearby acoustic sources or pulsatile flow. In literature, considerable attention has been devoted to different vortex shedding modes that arise due to the alteration of natural vortex shedding by such excitations, and associated nonlinear phenomena such as synchronization, hysteresis and chaos. (See, for example, Williamson and Govardhan, 2004; Griffin and Hall, 1991; Detemple-Laake and Eckelmann, 1989). Understanding such phenomena is important for practical problems such as control of vortex-induced vibrations.

* Corresponding author.
E-mail address: amit.agrawal@iitb.ac.in (A. Agrawal).

https://doi.org/10.1016/j.jfluidstructs.2019.102706
0889-9746/

A large number of studies, both experimental and numerical, indicate that for several forced vortex-shedding modes, the mechanism of formation is inherently two-dimensional. Couder and Basdevant (1986) observed a variety of vortex-shedding modes 2S, P+S, 2P, P and a symmetric mode in their two-dimensional thin-film experiments, for a velocity perturbation parallel to the flow. Detemple-Laake and Eckelmann (1989) found several vortex-shedding modes 2S, P, 2P, a symmetric mode and wake modulation at relatively low Reynolds numbers between 50 and 150 under inline acoustic excitation, for which three-dimensionality in the wake is unlikely to manifest. The 2P+2S mode, observed by Williamson and Roshko (1988) as a subharmonic in forced transverse vibration for $500 < Re < 1000$, was also observed at a much lower Reynolds number of $Re = 100$ by Krishnan et al. (2016) for inline pulsatile flow, and for acoustic excitation parallel to the flow by Detemple-Laake and Eckelmann (1989), again at a low Reynolds number. Konstantinidis and Balabani (2007) have compiled experimental results from the literature on the occurrence of symmetric modes for inline excitation. The Reynolds number for which a symmetric mode was observed ranged from 152 to 40 000. Srikanth et al. (2011) and Krishnan et al. (2016) have observed a symmetric mode in two-dimensional numerical simulations for rectangular and square cylinders, respectively.

The symmetric vortex shedding mode is particularly interesting in that when it occurs, the external excitation imposes completely and dominates natural vortex shedding. Several authors have studied the formation of symmetric vortex shedding due to its importance in inline vibration of bluff bodies. Naudascher (1987) identifies that during symmetric vortex formation, the shear layer forms closer to the base wall and the fluid accelerates towards the base wall during part of a cycle. He associates this with the relative movement between the bluff body and the wake, referring to this periodic phenomenon as wake breathing. Xu et al. (2006), Al-Mdallal et al. (2007) and Srikanth et al. (2011) identify the opposite-signed vorticity generated at the rear wall and attribute differing reasons for the production of base wall–vorticity. Xu et al. assume that the vorticity generation due to the acceleration term is important and must be comparable to the pressure-gradient based vorticity generation without excitation, for the symmetric shedding mode to occur. Al-Mdallal et al. attribute the base-region vorticity to the shear-layer instability. Both Xu et al. and Al-Mdallal et al. use a circular cylinder for which the two terms of vorticity production are difficult to discern. Srikanth et al. attribute the generation of base-wall vorticity to a ground effect, whereby the close formation of the shear layer nearer to the base wall induces strong secondary vorticity, indicating that the pressure-gradient based vorticity generation is responsible for the secondary vorticity. The results of Naudascher and Srikanth et al. rather point to a strong pressure gradient generation, responsible for base-region vorticity. While Naudascher emphasizes that the relative motion is important, Srikanth et al. emphasize the importance of the vorticity wall interaction. Thus several incomplete descriptions of the mechanism of the symmetric mode formation are available in literature.

From the observation that several different forced vortex-shedding modes occur under two-dimensional conditions, it can be expected that alterations to the natural vortex-shedding mechanism under forced excitation can be described using the two-dimensional vorticity transport equation, for such cases. Various studies available in literature regarding symmetric vortex shedding indicate that the mechanism of formation remains the same across different bluff bodies. A comparison of the visualizations of symmetric vortex shedding provided by Al-Mdallal et al. (2007) for a circular cylinder, Srikanth et al. (2011) for rectangular cylinders and by Krishnan et al. (2016) for a square cylinder show that the vortex shedding mechanism is very similar for different bluff bodies. In the present work, we systematically explore the vorticity dynamics of a square cylinder experiencing inline pulsatile flow at low Reynolds numbers, especially for the symmetric vortex-shedding mode, to clarify the nature of vorticity production and transport under inline pulsatile flow. The square cylinder is chosen because its faces are either aligned in the streamwise or cross-stream directions only, which simplifies the analysis considerably.

The layout of the paper is as follows. In the next section, the problem and numerical methodology employed for obtaining flow solution are described. In the subsequent sections, the vorticity transport equation and the mechanism of generation of vorticity at the surface is reviewed briefly to provide a clear perspective of the inherent vorticity kinematics and dynamics. The vorticity dynamics of symmetric vortex shedding and other modes are interpreted in accordance with the two-dimensional vorticity-transport equation, before summarizing the main findings.

2. Numerical methodology

In the present study, inline excitation is provided by employing velocity of the form $u = u_m + u_f\, sin(2\pi f_e t)$ and $v = 0$ at inlet, and on the lateral sides. At the outlet, the convective boundary condition is employed. Flow is initially assumed to be at rest. The flow domain along with the initial and boundary conditions employed in the simulation is given in Fig. 1. The domain size was chosen to be 15 D at the inlet and on the lateral sides. The outlet is kept at 55 D from the square cylinder rear side. The evolution of flow variables is computed using *D2Q9* Lattice Boltzmann Method with a single relaxation time and BGK operator (See Succi, 2001; Chen and Doolen, 1998 for further reference).

The evolution of flow field is computed in the following manner: the particle distribution function at each node is initialized to the equilibrium value corresponding to the initial values of the flow variables. The evolution of particle distribution functions is tracked by lattice propagation step given in Eq. (1) and collision step given in Eq. (2)

$$f_i\left(\vec{x}+\vec{e}_i, t+\delta_t\right) = f_i^n\left(\vec{x}, t\right) \tag{1}$$

$$f_i^n\left(\vec{x}, t\right) = f_i\left(\vec{x}, t\right) - \left(f_i\left(\vec{x}, t\right) - f_i^{eq}\left(\vec{x}, t\right)\right)/\tau \tag{2}$$

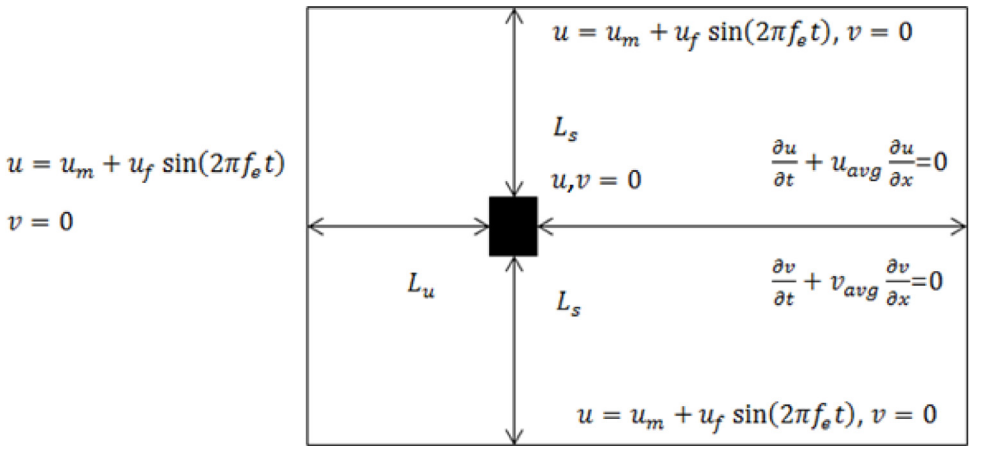

Fig. 1. Initial and boundary conditions for flow past the square cylinder that is subjected to inline pulsation. Domain size, $L_u = 15D$, $L_d = 55D$, $L_s = 15D$.

Table 1
Summary of various validation cases conducted using present LBM code.

Reference	Validation problem	Comparison with literature
Kumar et al. (2008)	Laminar vortex shedding of square cylinder under steady inflow	Drag and Strouhal number validated with Sharma and Eswaran (2004), Robichaux et al. (1999), Sohankar et al. (1997), Franke et al. (1990)
Sewatkar et al. (2011)	Laminar vortex shedding of square cylinder under transverse oscillation	Drag and Strouhal number compared with Tanida et al. (1973)
Krishnan et al. (2016)	Laminar vortex shedding of square cylinder under steady inflow	Base pressure coefficient compared with Sohankar et al. (1997)
Krishnan et al. (2018)	Laminar oscillatory flow of a square cylinder flow	Drag coefficient compared with Bearman et al. (1985) and Scolan and Faltinsen (1994)

where $f_i^n\left(\vec{x}, t\right)$ and f_i^{eq} are the post-collision distribution function and equilibrium density function at a node. The latter function is computed as:

$$f_i^{eq}\left(\vec{x}, t\right) = \rho w_i \left(1 + 3\left(\vec{e}_i.\vec{u}\right) + \frac{9}{2}\left(\vec{e}_i.\vec{u}\right)^2 - \frac{3}{2}(\vec{u}.\vec{u})\right) \tag{3}$$

where ρ denotes the macroscopic density at the node; $\vec{u}$ denotes the macroscopic velocity vector; $\vec{e}_i$ denotes the lattice vectors of the *D2Q9* scheme; and w_i denote the lattice constants for each lattice vector. The parameter $\tau$is the relaxation time and is linked to the kinematic viscosity as $\vartheta = (2\tau - 1)/6$. At the boundaries, the equilibrium distribution functions are computed after the collision step, from the known value of macroscopic variables and propagated to the next step. On the wall, the no slip boundary condition is implemented using the bounce back scheme (See Agrawal and Agrawal, 2006, for details of implementation). At each time step, the macroscopic variables are recovered from the known distribution functions by using Eq. (4).

$$\rho = \sum_{i=0-8} f_i, \qquad \rho\vec{u} = \sum_{i=0-8} f_i\vec{e}_i, p = \rho C^2 \tag{4}$$

where p denotes the macroscopic pressure, and C is the lattice speed of sound for the *D2Q9* scheme.

A summary of various validation cases conducted using present LBM code is given in Table 1. The present code has been validated extensively for steady inflow problem by Kumar et al. (2008) and unsteady oscillation problems by Sewatkar et al. (2011). In our previous work, we have discussed (Krishnan et al., 2016) the flow regime map and spectral analysis of various vortex shedding modes of a square cylinder that is subjected to inline pulsatile flow. The results compare favorably with the experimental results of Detemple-Laake and Eckelmann (1989) for a circular cylinder that is subjected to an inline excitation imposed over mean flow. In an, another related work, the discussion of the lift and drag coefficients of various forced vortex shedding modes and its correlation with the evolution of various circulation regions, including symmetric vortex shedding is given by Krishnan et al. (2018).

For the present study which deals with the vorticity transport around the bluff body, the vorticity field is computed by calculating the curl of the velocity field, where $\omega = \partial v/\partial x - \partial u/\partial y$. The differential terms for evaluating vorticity

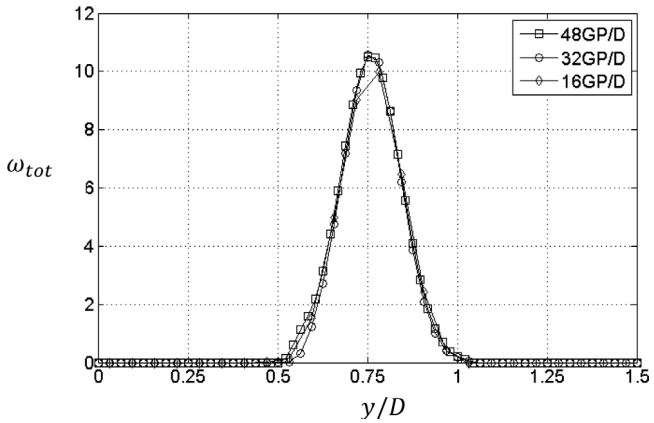

Fig. 2. Instantaneous spatial vorticity flux profile for the symmetric vortex shedding mode observed at *Re*= 100, f*= 0.126 and A* = 0.6 for different grid resolutions. The positive vorticity flux into the wake is plotted at the time instant when the total vorticity flux in to the wake is maximum.

are calculated using central differencing scheme, in the interior of the fluid domain. Near the boundary, the vorticity at the known interior fluid nodes are extrapolated on the bounce back nodes using quadratic polynomial. From the known vorticity field, the circulation regions of interest are computed by first isolating the vortical regions in the control volume and then subsequently evaluating the expression $\Gamma = \iint \omega dA$ numerically. For numerical integration, along both directions, Simpson's rule is employed. The diffusive flux of vorticity is calculated numerically using central differencing scheme to evaluate the derivatives of vorticity normal to the control volume. The convective flux of vorticity obtained directly from the velocity and vorticity profiles on the boundary of the control volume. The fluxes for each vorticity sign are calculated separately and the sign of convection is assumed to be along the flow direction irrespective of the sign.

To check the spatial convergence of solution, the total instantaneous positive vorticity flux (ω_{tot}) profile through the nondimensionalized x-coordinate $x/D = 0.5$, is plotted for different grid resolutions in Fig. 2, for the symmetric vortex shedding mode observed at *Re*= 100,f^*= 0.126 and A^* =0.6 (See Krishnan et al. for detailed flow regime map). The positive vorticity flux into the wake is plotted at the time instant when the vorticity flux in to the wake is maximum. Note that origin of coordinate system is fixed at the center of the square cylinder and direction of x-axis is same as inflow direction. The net vorticity flux into the wake computed using the Simpson's rule based spatial integration of vorticity flux profile for different grid resolutions show that the difference in vorticity flux into the control volume is less than 1% between 32 and 48 GP.

3. Vorticity generation and transport under two-dimensional flow

For the two dimensional flow of a barotropic/incompressible fluid over a solid bluff body, the vorticity transport is given by Eq. (5) (Morton, 1984; Wu and Wu, 2006). The scalar nature of the two-dimensional transport equation (5), lends itself to an interpretation of vorticity as a (diffused) passive scalar.

$$\underbrace{\frac{\partial \omega}{\partial t}}_{\text{Local derivative}} + \underbrace{u.\nabla\omega}_{\text{Convective term}} - \underbrace{\nu\,\nabla^2\omega}_{\text{Diffusive term}} = 0 \tag{5}$$

For a barotropic/incompressible flow, there are no sources of vorticity within the fluid, and all vorticity must be generated at solid boundaries and then transported by diffusion and convection into the flow domain. For the problems considered here, the external fluid boundary is placed far away from the solid body walls and it is useful to impose that $\omega = 0$. Any vorticity must be produced at the walls of the rigid body. Morton (1984) provided a useful expression for the instantaneous vorticity flux from solid walls of a rigid body undergoing bluff-body motion as well as subject to a fluid flow. The expression for the instantaneous vorticity flux from a differential element along a solid wall is given by Eq. (6).

$$\left(\nu\frac{\partial\omega}{\partial n}\right)_t = \left(\underbrace{\hat{n}\times\vec{a}}_{I} + \underbrace{\hat{n}\times\frac{1}{\rho}\frac{\partial p}{\partial \hat{s}}}_{II}\right)_t . \tag{6}$$

In Eq. (6), $\hat{n}$ denotes unit vector normal to wall, $\hat{s}$ denotes unit vector tangential to the wall and $\vec{a}$ is the rigid body acceleration of the bluff body. Here, term I on the RHS of Eq. (6), gives the vorticity generation due to the bluff-body acceleration. The term II on the RHS represents vorticity generation due to an instantaneous tangential pressure gradient

acting on the differential element. The boundary vorticity flux is essentially a nonlinear, solution dependent, Neumann-type boundary condition that is difficult to evaluate *a priori*. In formulations such as the vorticity-stream function approach to solve for flow variables, this unsteady flux is computed using the information available about the stream function and derivatives at the wall and is not calculated explicitly.

While it is difficult to evaluate the vorticity flux from the wall explicitly for flow under general excitation, a few qualitative judgments can be obtained by considering the nature of both terms for different bluff body shapes. Consider the vorticity flux from circular, square and rectangular bluff bodies that oscillate sinusoidally in the in-line direction, due to term I in Eq. (6). For a circular cylinder, the direction of the wall normal and the inline acceleration direction vary across the body and hence the vorticity flux is spatially non-uniform and maximum at the top and bottom of the cylinder at a given instant. The sign of the vorticity flux from the wall also alternates depending on the direction of acceleration. Although over a full cycle the net circulation produced is zero, it can be shown that over a half cycle and over the top/bottom half perimeter from the front to the rear stagnation points, the net circulation from the wall due to the acceleration term is $2u_f D$. Here, $u_f = A\omega$ is the amplitude of the relative velocity of the bluff-body motion due to the inline excitation and D is the diameter of the cylinder. For a square cylinder, the vorticity flux is spatially uniform and unsteady at the top and bottom walls, and vorticity generation in the front and rear walls due to acceleration is zero, as per equation (6). The circulation generated over a half cycle and at the top or bottom wall is also $2u_f D$, where D is the side length of the square cylinder. It can be observed that the magnitude of circulation generated due to acceleration is proportional to the projected area normal to the direction of acceleration. Furthermore, this implies that for bluff bodies such as normal flat plates under in-line excitation, the magnitude of circulation generated from this mechanism is almost zero.

The tangential pressure gradient around a bluff body can also be considerably altered under dynamic flow conditions, and the contribution of term II in Eq. (6) to the net vorticity flux could be significant. It can be assumed that the relative motion between the fluid and bluff body should also cause unsteady vorticity generation, dependent on the relative fluctuating motion between bluff body and flow. Another mode of vorticity generation, which is due to term II in Eq. (6), is the generation of circulation at the wall when a pre-existing circulation region interacts with a wall. A good example for this mode of vorticity generation is the impingement of a vortex pair on a stationary wall. Since for a stationary wall, there can be no vorticity generation from term I in Eq. (6), the secondary vorticity generated near wall must be due to the altered tangential pressure gradient at the surface due to impinging circulation (Naguib and Koochesfahani, 2004; Cheng et al., 2010).

Few authors have considered the nature of the boundary flux from the wall under excited conditions alone. Blackburn and Henderson (1999) attributed the weak chaos observed in their study of transverse vibration to the competition between acceleration and pressure-gradient based generation in the base region. Xu et al. (2006) suggested that different modes result from the superposition of the mechanism of unsteady vorticity generation due to acceleration and the mechanism of relatively constant pressure-gradient based vorticity generation. In our previous work (Krishnan et al., 2016), we have shown that there is no a priori reason to assume that pressure gradient based vorticity generation has to be constant under excited condition. For a better description of the vortex-shedding mechanism, the alteration of the velocity field and the associated change in the nature of vorticity transport around the bluff body also needs to be accounted for.

In the present work, we study the inline pulsatile flow of a square cylinder for fixed amplitude and frequency of excitation to understand vorticity transport around the bluff body for symmetric vortex shedding conditions. This is to allow the mechanism of vortex shedding under excited condition to be described in similar spirit to that of Gerrard (1966). A pulsatile flow with a mean flow is kinematically equivalent to the in-line vibration of square cylinder under a mean flow (Perdikaris et al., 2009; Srikanth et al., 2011). By fixing the amplitude ratio and frequency, it can be expected that contribution of term I in Eq. (6) on the vorticity dynamics will remain similar for different cases considered here. By varying the Reynolds number, one would expect that the pressure-gradient-based generation term II in Eq. (6) will vary strongly. Using a square cylinder clearly demarcates the different regions of vorticity production and the symmetric vortex shedding is most apt as this mode entails complete imposition of the excitation. However, for sake of completion, before proceeding to examine the excited condition, the vorticity transport and circulation balance in the wake is described for steady inflow without pulsation at a low Reynolds number.

4. Vorticity transport under steady inflow

The mechanism of natural vortex shedding described by Gerrard (1966) is briefly reviewed here. Gerrard's mechanism can be understood with reference to Fig. 3. Consider a growing vortical region on the upper side of the bluff body. This strong vortical region draws fluid across the wake. This drawn fluid separates into three branches indicated as 'a', 'b' and 'c' in Fig. 3. The fluid drawn across as 'a' feeds into the growing pre-shed vortex. A part of the transported fluid 'b' severs the supply of shear-layer circulation convecting from the surface, while fluid 'c' feeds in anticlockwise circulation to the newly forming vortex, which becomes stronger over a time period. This increase in vorticity strength of the bottom vortex and severing of the vorticity supply to the upper vortex imply that fluid will be drawn from the upper side in opposite in direction during the next half cycle, weakening the vorticity strength of the lower shear layer and allowing the cycle to repeat.

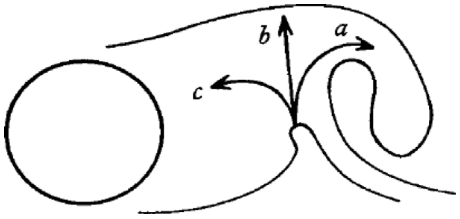

Fig. 3. Entrainment mechanism leading to vortex shedding (Gerrard, 1966).

The vorticity transport under steady inflow in the near wake of the bluff body for a low Reynolds number 100, can be interpreted, in accordance with Eqs. (5) and (6). For the steady inflow considered at $Re = 100$, the vorticity generation and transport is characterized by a relatively steady vorticity generation near the bluff body walls and strong unsteady vorticity redistribution in the near wake due to transverse entrainment of the flow. Only pressure-gradient-based vorticity generation occurs for steady inflow and most of the vorticity generation takes place around the front sharp corners for square cylinder. The vorticity generated after the separation point, which must be opposite in sign compared to the adjacent shear layer, will slightly decrease the strength of the main shear-layer vorticity. However, this vorticity is small and is not expected to have any significant role in the natural vortex-shedding mechanism. The vorticity generated and convected into the shear layer is subjected to considerable diffusive annihilation at the interface of the oppositely signed circulation region. Vorticity that survives cross-annihilation in the near wake is convected into the wake, in each half cycle, and finally diffuses outwards into the adjacent, oppositely signed vortical regions.

In the present study, the vorticity transport for a square cylinder under natural vortex shedding is carried out for $Re=$ 100, in contrast to Gerrard. Due to the strong entrainment phenomenon, vorticity transport in the wake is inherently unsteady for $Re = 100$. The transverse component of velocity, which is indicative of strong entrainment, is plotted along the wake centerline and is shown in Fig. 4(a) for two time instants T1 and T2 over a cycle, at which the cross-stream velocity is maximum. The maximum cross-stream velocity occurs at a distance of $x/D = 3.0$, (shown as MP1 in Fig. 4 a). For $Re = 100$, the vorticity contours and velocity-vector plots are shown in Fig. 4(b) at the time instant T1. Here, the relative spacing of vorticity contours marks the intensity of the diffusive flux, while the velocity vectors indicate the direction of transport of vorticity due to convection. Thus, a good visualization of vorticity transport process can be obtained in a single frame. The red arrows indicate the evolution of the flow according to Gerrard's mechanism, for a square cylinder. The branch 'b' completely severs the supply of circulation from the boundary layer, as shown in Fig. 4(b). The nondimensionalized vorticity profile along the bluff body walls, $\omega_w = \omega D/u_m$, is plotted at the front, top, bottom and back walls in Fig. 5(a) and (b), indicating how the different regions contribute to vorticity production. The surface vorticity value is evaluated by numerically extrapolating using a quadratic polynomial from the adjacent fluid nodes. The main difference in the wall–vorticity profile between two frames is due to the unsteady vorticity generation at the rear wall. The strength of this base wall circulation region is negligible.

The vorticity transport in the wake is illustrated using a control volume JGHI. Within this control volume, both separating shear layers interact to produce vortices of opposite sign in each cycle. Positive vorticity is transported into the control volume through the upper side CG and negative vorticity is transported into the control volume through the lower side JD. There is no vorticity transport through the upper side GH and lower side JI. Vorticity escapes only through the face HI. The HI face is located at a distance where the fluid branch 'b' cuts off supply to the shear layer. Gerrard (1966) identifies two characteristic lengths for the vortex shedding process, the first is the width to which vorticity diffuses at the separation point, l_d and the second is the vortex formation length scale l_f. In the present case both can be easily identified with the chosen control volume. The thickness of positive/negative vorticity profile on side JG, denote the diffusive length scale while the distance of the control volume HI from base wall is the vortex formation length scale. By applying vorticity balance on the control volume one can estimate the amount of vorticity that survives the entrainment process.

For circulation balance, the integral form of Eq. (5) is applied over control volume JGHI. The integral form of the equation is given in Eq. (7) below where, the rate of change of net circulation, $\Gamma = \int\int \omega dA$, inside a fluid region is balanced by the line integral of vorticity flux through the bounding surface of the region:

$$\frac{\partial \Gamma}{\partial t} + \oint \left(\vec{u}\omega - \nu \frac{\partial \omega}{\partial n} \right) .d\hat{s} = 0 \tag{7}$$

Consider the positive vorticity that enters into the control volume through face JG. The nondimensionalized convective flux profile $\omega_{f,c} = u\,(y)\,\omega\,(y)\;\; D/u_m^2$ and the nondimensionalized diffusive flux profile $\omega_{f,d} = \nu(\partial\omega/\partial n)\,D/u_m^2$, which enter into the control volume through the upper side CG is shown in Fig. 5(c). Here $u(y)$ and $\omega(y)$ are the velocity and vorticity profile along face JG. The vorticity transport into the control volume due to diffusion is much less than convection. There is no vorticity generation within the control volume. The strength of the small circulation region near the base wall is less than 3% of the shed vorticity and thus is not considered significant. The total positive circulation transported into the wake at an instant can be obtained by spatially integrating the convective and diffusive transport fluxes $\omega_{tot} = \omega_{f,c} + \omega_{f,d}$

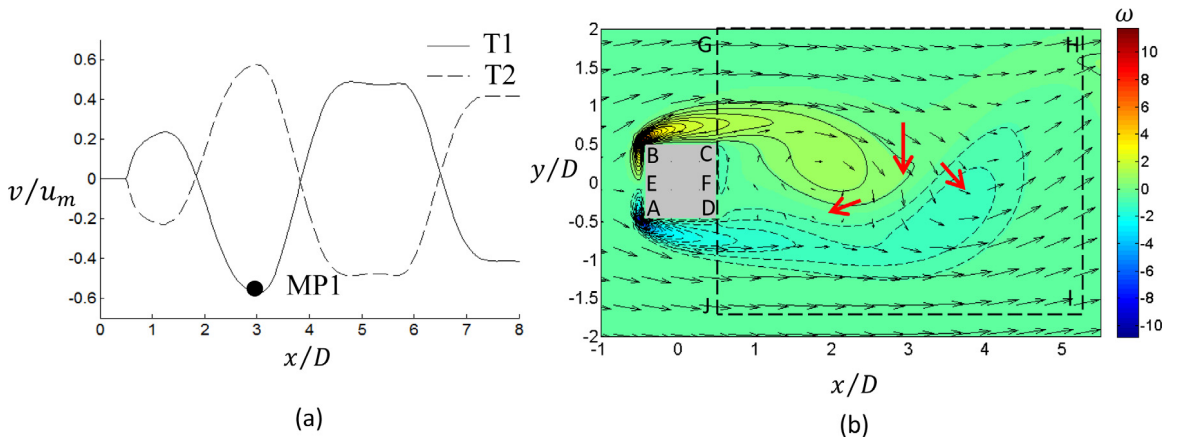

Fig. 4. (a) Cross-stream wake velocity plot along wake centerline, for $Re = 100$ when the wake velocity magnitude is maximum at time instants T1 and T2 (b) Vorticity contour and velocity vector plots when wake cross-stream velocity is maximum along wake centerline for $Re = 100$ at time instant T1. The solid red arrows indicate flow branches in the near wake of square cylinder, similar to Gerrard's description for circular cylinder (1966).

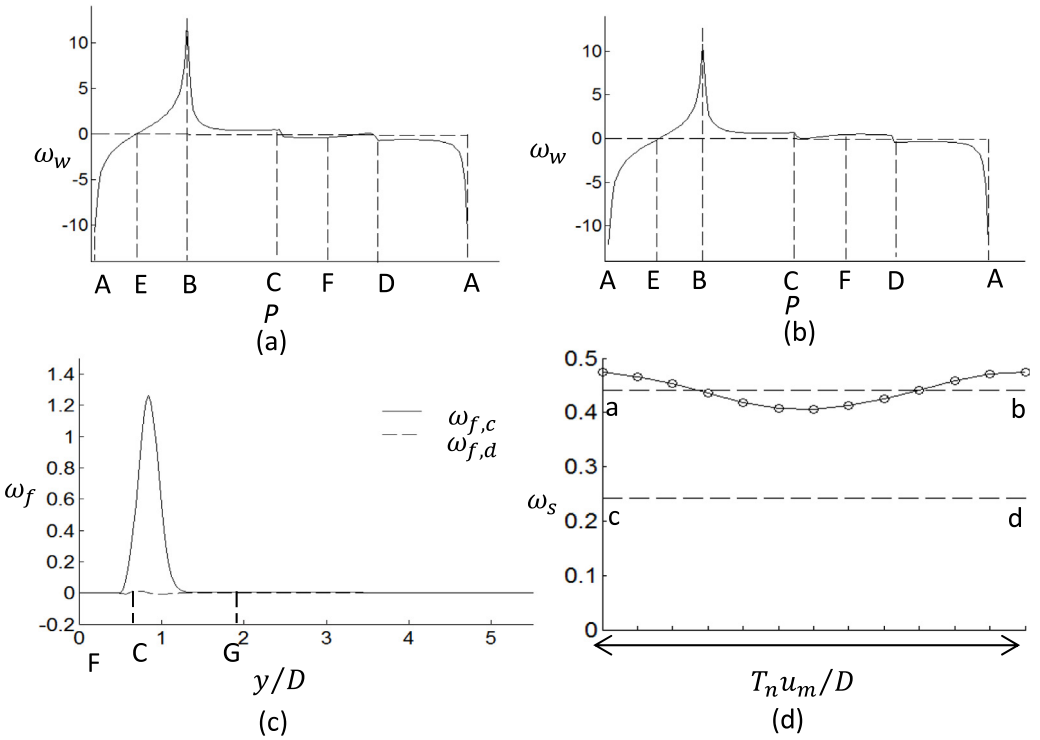

Fig. 5. (a) Wall–vorticity value of a square cylinder around periphery, P for Re = 100 at time T1. (b) Wall–vorticity of square cylinder at time T2. (c) Convective and diffusive fluxes through the face CG of the control volume JGHI. (d) Spatially integrated total vorticity flux, over a cycle. For the location of various points indicated in graphs, refer Fig. 4(b).

through the boundary layer. The spatially integrated vorticity flux into the control volume defined as $\omega_s = \int_{y_C}^{y_G} (\omega_{tot})\, dy$, is plotted over the entire vortex shedding cycle in Fig. 5(d). All the quantities are nondimensionalized appropriately and it is ensured that the y coordinate of the point G, y_G, is greater than the diffusion length l_d so that all the vorticity into the control volume is accounted for. The spatial integration was done numerically using Simpson's rule. In Fig. 5(d), it can be observed that the vorticity transported into the wake is not exactly steady. This is to be expected, since as some amount of fluid is drawn across the wake, the boundary layer will be affected and will have some bearing on the flux into the control volume.

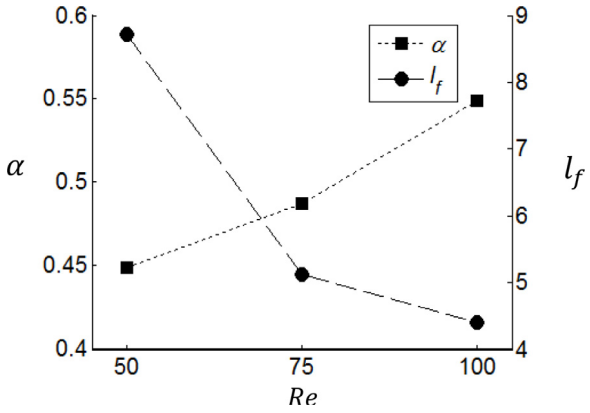

Fig. 6. Fraction of vorticity survived (α), formation length (l_f) vs. *Re* for square cylinder.

By integrating the spatially integrated vorticity flux, ω_s, over a vortex-shedding cycle, one can obtain the net circulation transported into the control volume, denoted as Γ_{tot}, and by knowing the circulation strength of the shed vortex Γ_v, immediately after the vortex shedding process, one can estimate the fraction of circulation that survives the entrainment process. The $\Gamma_{tot} = \int_0^{T_n} \omega_s dt$ is evaluated numerically using Simpson's rule and the strength of the shed vortex $\Gamma_v = \iint \omega dA$, is evaluated numerically over the spatial region extended across the shed vortex, immediately outside the control volume. In Fig. 5(d), the area under the line 'ab' gives the net positive vorticity transported into the control volume and area under the curve 'cd' gives the circulation that is shed into the wake. The *y*-ordinate of 'ab' and 'cd' gives the time-averaged flux into the control volume and time-averaged flux out of the control volume respectively, for positively signed vorticity. The ratio of the areas under line 'ab' and line 'cd' gives the fraction of circulation, α that survives the entrainment process.

In Fig. 6, the α and l_f are plotted over the *Re* range investigated in the present study. It is estimated that for $Re = 100$, the fraction of vorticity that survives the entrainment process, denoted as α is 0.55. It can be observed from figure that the α varies from 0.45 to 0.55, from $Re = 50$ to $Re = 100$. The length of the vortex formation region, l_f decreases from 8.7 for $Re = 50$ to 4.4 for $Re = 100$. This reduction in formulation length is correlated to higher natural vortex shedding frequency at high $Re = 100$.

While no explicit comparison could be obtained for square cylinder from literature, the typical value of α ranges from 0.2 to 0.6 depending up on the bluff-body type and Reynolds number (Bearman, 1984). Abernathy and Kronauer (1962) computed the value of α to be 0.6, for two parallel shear layers of opposite vorticity without the presence of a bluff body, implying that the role of bluff body in natural vortex shedding is mainly to supply circulation into the shear layers. This independence of natural vortex shedding mechanism to the bluff body shape had led to concepts such as universal Strouhal number where by one takes a characteristic length such as l_d to define the Strouhal number rather than the bluff-body dimension.

5. Vorticity transport under pulsatile inflow

The mechanism proposed by Gerrard (1966) is essentially an interpretation of the 2D vorticity transport equation with the implicit assumption that the vorticity transport into the wake from the separating shear layers is relatively steady. The motivation for Gerrard to propose his mechanism of natural vortex shedding was to explain the discrepancy in Strouhal number observed between his results and Roshko's (1954) results for similar Reynolds numbers. Gerrard attributed this to the differing l_d due to the differing turbulent intensity between their experiments. In the strictest sense, the mechanism proposed by Gerrard is incomplete, in that it already assumes the velocity profile as given. The mechanism gives only a two-dimensional picture, although the vorticity transport is three dimensional at the Reynolds numbers considered. The scalar nature of the 2D vorticity transport equation does not reveal the full nature of coupling between the velocity and vorticity fields. Also, the flow solution-dependent vorticity production is implicitly assumed as constant at a given Reynolds number. However, the advantage of the description of Gerrard is that it allows one to identify characteristic flow features associated with the natural vortex-shedding mode and also to understand the implication of flow control elements such as a splitter plate that disrupts the vorticity transport in the near wake. A relevant question to ask is how the 2D nature of the vorticity transport equation coupled with the boundary generation term can be used to understand the mechanism of vortex shedding, under forced excitation condition, an approach similar in spirit to the description of Gerrard.

In the present work, a pulsatile flow of the form $u = u_m + u_f \sin(2\pi f_e t)$, is imposed at the inlet to alter the natural vortex-shedding mechanism of a square cylinder. One advantage of using a square cylinder is that any vorticity production

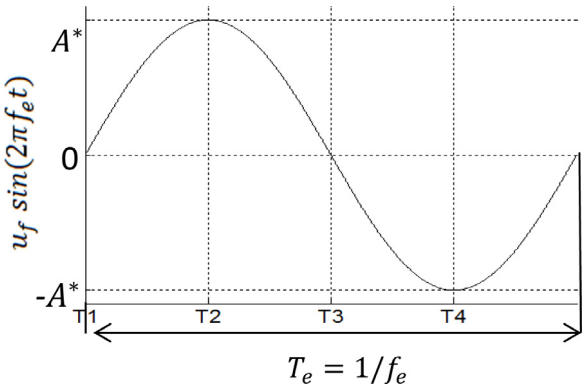

Fig. 7. Timing of inline pulsation over a cycle, showing snapshot times T1, T2, T3 & T4.

due to relative acceleration of the fluid should only appear on the top and bottom surfaces of the bluff body and cannot appear on either front or rear faces. Thus, a square cylinder under inline pulsatile flow can help discern the vorticity production due to different boundary source terms in a more definite manner than is the case for a circular cylinder.

The three non-dimensional parameters relevant to the problem considered here are Reynolds number based on mean flow $Re = u_m D/\nu$; amplitude ratio $A^* = u_f/2\pi f_e D$; and frequency ratio $f^* = f_e D/u_m$. First, the alteration to vorticity transport for $Re = 25$, $A^* = 0.6$ and $f^* = 0.126$ is discussed relative to the unperturbed case. The choice of amplitude and frequency ratio may appear somewhat arbitrary but this is not the case. Krishnan et al. (2016) have observed the symmetric vortex-shedding mode under harmonic lock-in condition, for this amplitude and frequency ratio at Re = 100. The value of f^* is 0.9 times the natural vortex-shedding frequency at $Re = 100$, and the flow parameters lie at the left side of the synchronization region centered at approximately $f^* = 0.14$. As a corollary to the fact that the imposed excitation completely dominates at this amplitude and frequency ratio at $Re = 100$, it can be expected that at lower Reynolds numbers where natural vortex shedding is less vigorous or non-existent, the excitation will readily dominate over natural vortex shedding, if present. By keeping the frequency and amplitude ratio the same and examining the vorticity transport for a different Reynolds number, the pressure-gradient dependent nature of vorticity generation under excitation can be studied and compared.

Due to the unsteady nature of vorticity transport and generation under the excited condition, first the effect of imposed excitation for $Re = 25$, $A^* = 0.6$ and $f^* = 0.126$ is discussed in detail. At this low Re, the vorticity generation and transport is steady for flow without excitation. The external excitation causes both unsteady vorticity generation as well as unsteady transport into the wake. In Fig. 7, the external excitation waveform is given and the points at which snapshots are taken are indicated and marked. In the present study the timing of vortical events are reported with respect to inline pulsation cycle, similar to Konstantinidis and Balabani (2007). In all subsequent figures, the timing of snapshots is referred to Fig. 7. To get a clear picture of the nature of the vorticity generation and transport, the snapshots of superimposed velocity and vorticity contours for $Re = 25, A^* = 0.6, f^* = 0.126$ at four time instants T1, T2, T3 and T4, are shown in Fig. 8(a)–(d).

The snapshots of the velocity and vorticity contours under excited conditions show notable differences compared to those for steady inflow at $Re = 25$. From Fig. 8(a), it can be observed that the vorticity generation on the rear wall is enhanced and that there is strong unsteady counter-current flow in the wake at the start of the cycle. This strong counter-current flow encounters the base wall and is deflected towards the y-direction while carrying vorticity of opposite sign to that of main shear layer (See Fig. 8b–d). This counter-current flow is split into two components, indicated by red arrows in Fig. 8(a), with one penetrating into the low velocity boundary layer while the one severs the vorticity supply to the downstream. Later in the cycle, this strong counter-current flow wanes, which allows the boundary layer flow to recover near the wall, and then once again the strong counter-current flow recovers strength and the cycle repeats.

The instantaneous wall–vorticity profile along the square cylinder perimeter at various instants is plotted in Fig. 9. At the start of the cycle at T1, vorticity is relatively large at the rear walls while the vorticity at the front corners is considerably less. This can also be confirmed from the snapshot of velocity and vorticity contours given in Fig. 8(a). The strong counter-current flow considerably disrupts the boundary layer and reaches far upstream. Gradually, the mean flow again starts to recover the boundary layer and vorticity generation at the front corners picks up. This recovery of the shear layer by the mean flow is evident in Fig. 8(b)–(d), and in the visualizations of wall–vorticity contours of Fig. 9(b)–(d). Note that although the pulsating amplitude is zero at instants T1 and T3, the wall–vorticity profiles are very different. This difference is due to the strong wake counter flow present at time T1, which considerably disrupts the vorticity production due to the mean flow. At time T3 the wake counter flow has waned and the shear layer is recovering from the effect of wake counter flow on the wall–vorticity production. The wall–vorticity on the side walls also fluctuates, however, the magnitude of fluctuations is smaller compared to that at the sharp corners.

The vorticity transport into the wake can be understood by considering a control volume shown, as FGHI as shown in Fig. 8(a). Before proceeding with accounting for various fluxes into and out of the control volume, it is useful to provide

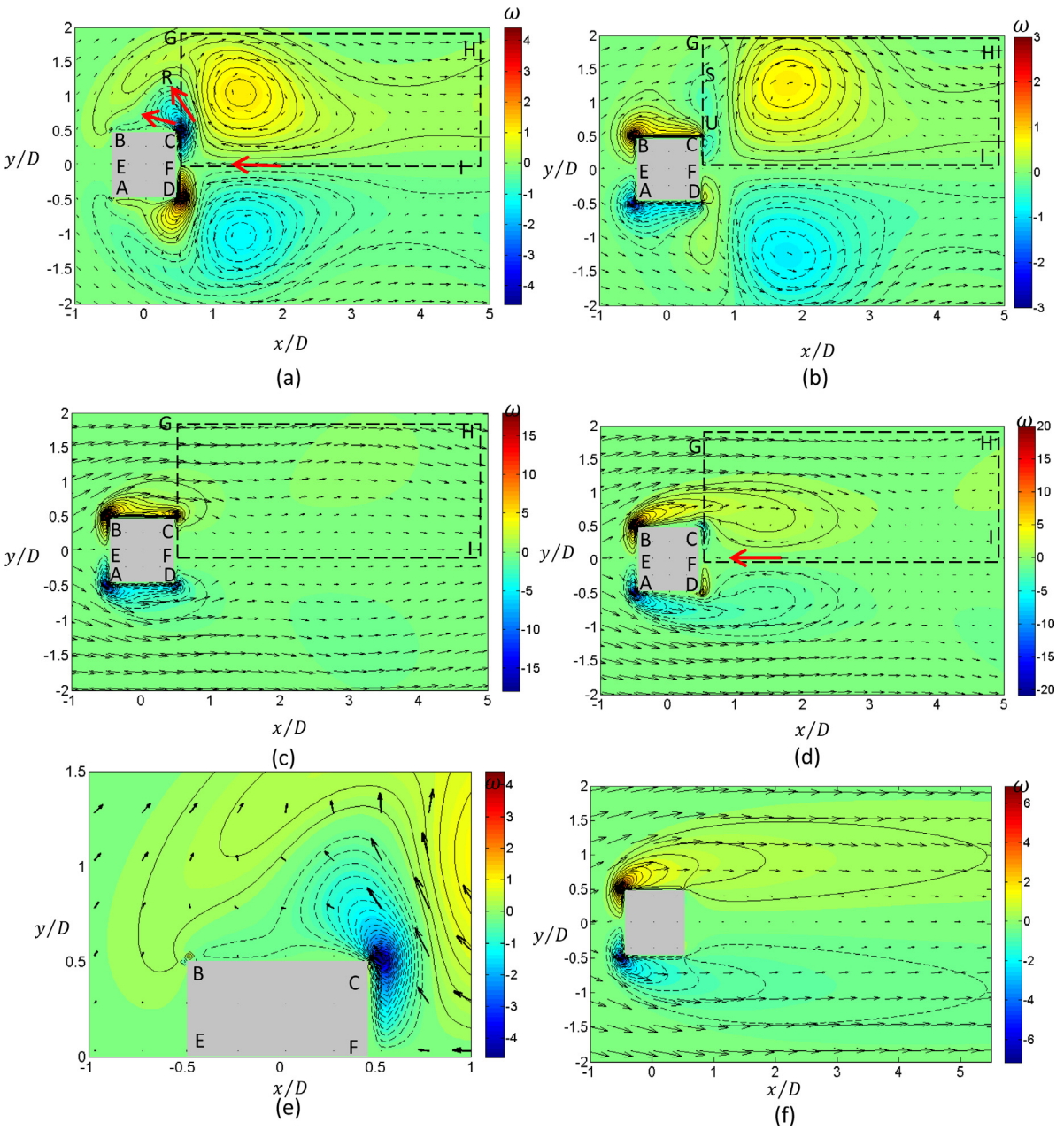

Fig. 8. (a)–(d). Vorticity contours and superimposed, velocity vectors shown at instants T1, T2, T3 and T4. Fig. 8(e) shows flow near sharp corner C at T1 (For timing of snapshots refer Fig. 7). In Fig. 8(f) the steady vorticity profile is shown for comparison. (For interpretation of the references to colour in this figure legend, the reader is referred to the web version of this article.)

some clarifications on the sign of vorticity transport. In the present case, it is assumed that vorticity is carried across boundaries as a passive scalar, and the direction of the convection of vorticity is dictated by the flow velocity alone and is independent of the sign of vorticity. Of course, the diffusive process is also independent of the sign. While accounting for vorticity flux into and out of the control volume, the positive and negative vorticity are accounted for separately. A gain of vorticity of either sign into the control volume is considered positive and a loss of vorticity of either sign in the control volume is considered negative.

The control volume FGHI, mainly encloses positive vorticity. However, there are no sources of positive vorticity and all the positive vorticity is transported into the control volume by the flow, from the upstream walls, through the face CG. There is, however, considerable transient negative vorticity generated at the rear wall by the counter-current flow. A fraction of this counter-current flow carries negative vorticity into the nearby boundary layer fluid and considerably

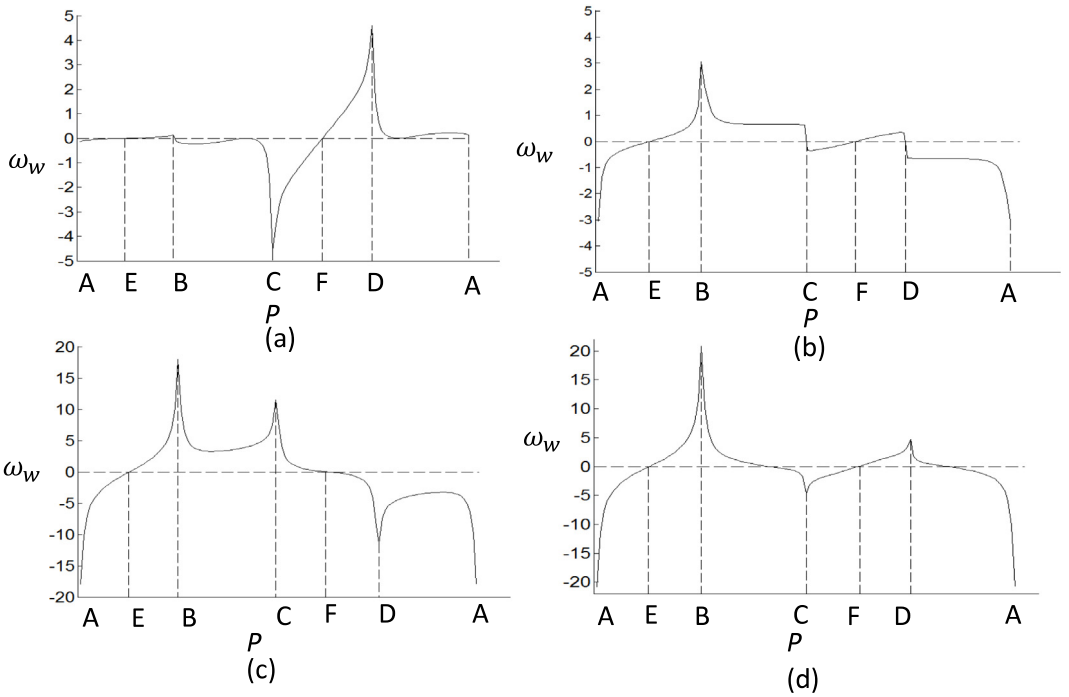

Fig. 9. Wall–vorticity profile of the square cylinder, along periphery P, at $Re = 25, A^* = 0.6, f^* = 0.126$, at various time instants in a shedding cycle: (a) T1; (b) T2; (c) T3; (d) T4.

disrupts the vorticity transport. In Fig. 10(a)–(d), both the convective and diffusive fluxes into the control volume are plotted at the time instants T1, T2, T3 and T4. In Fig. 10(a), positive vorticity is convected into the control volume through only a portion of the face CG, from R to G. From point C to R, negative vorticity is carried outwards from the control volume by counter-current flow. The diffusive flux is also outwards from the control volume and is appreciable in terms of negative vorticity. This is clearly evident in Fig. 10(a). In Fig. 10(b), it can be seen that positive vorticity enters through the boundary layer CS, as well as by the flow outside the boundary layer through UG. Between S and U, negative vorticity is down-washed into the control volume. Since a gain of either-signed vorticity is considered as positive, flux is positive for both signs at this instant. In Fig. 10(c) and (d), the negative vorticity is completely annihilated into the main positive vorticity, and only positive vorticity is carried into the control volume. The boundary layer due to the main flow recovers from the disrupting counter-current flow and positive vorticity is fed into the control volume. The positive vorticity in the control volume undergoes diffusive annihilation with the oppositely signed vorticity at the base region and the oppositely signed shear layer. The instantaneous diffusive flux through the wake center line is shown at time instants T1 and T3 in Fig. 10(a). In Fig. 11(a), the FM region shows the loss of negative base-region vorticity to the adjacent positive vorticity, while from M to I the positive vorticity is annihilated with the oppositely signed shear-layer vorticity. At instant T3 no negative circulation region is present and hence all the vorticity lost through this face is positive vorticity. In Fig. 11(b) the positive vorticity lost into the wake through face HI is plotted for instants T1 and T3.

In Fig. 12, snapshots of velocity and vorticity contours under inline excitation are shown at time instant T1, for both $Re = 50$ and $Re = 100$, for $A^* = 0.6$ and $f^* = 0.126$. The vorticity contour interval displayed in Fig. 12 consists of fifty equally spaced levels between vorticity maxima/minima for either sign. These snapshots are very similar to the snapshot shown in Fig. 8(a). The counter-current flow velocity profile along the wake center at instant T1 is shown in Fig. 13(a), for different Reynolds numbers. It can be observed from Fig. 13(a), that as a result of the increase in Re, the intensity of counter-current flow increases, and is higher than the relative velocity of the mean flow and fluctuating velocity combined. In fact at $Re = 100$, the counter-current flow velocity is twice that of the mean velocity, even though there is no reverse flow at the inlet.

The strong counter-current flow encounters the rear wall and splits into an upward and downward branch in a symmetrical fashion. The deflected flow is characterized by the transverse velocity profile through the plane CN within the control volume FGHI and is shown in Fig. 13(b). The positive transverse velocity through face CN adjacent to the sharp corner is due to the strong counter-current flow, and is almost similar in magnitude as that of the counter-current flow, indicating hardly any momentum loss. In Fig. 13(c) the velocity profile through the face FG is shown. The reverse flow upstream through the boundary layer is proportional to the deflected flow. A part of the deflected fluid flow penetrates into the low velocity boundary layer and the momentum of which is lost subsequently as the main flow boundary layer

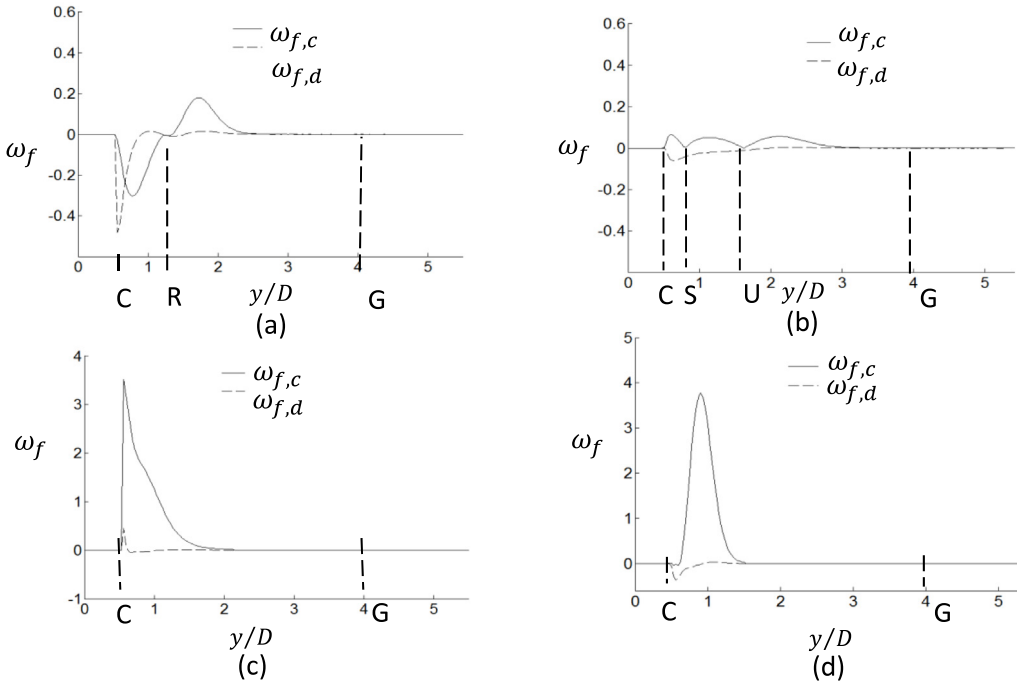

Fig. 10. Vorticity-flux profile through the control volume face CG at $Re = 25, A^* = 0.6, f^* = 0.128$, at various time instants: (a) T1; (b) T2; (c) T3; (d) T4. Note that, change in y-ordinate scale for (c) and (d) is one order higher compared to (a) and (b).

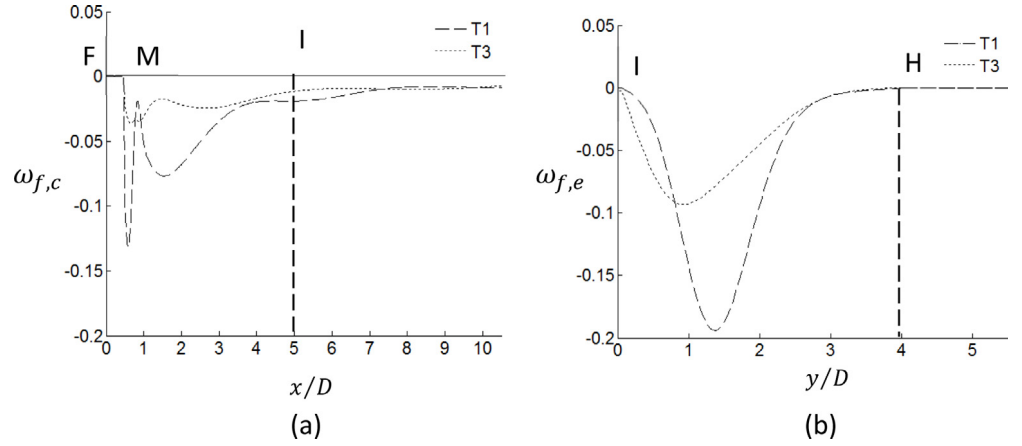

Fig. 11. Instantaneous vorticity-flux profile through control volume faces at $Re = 25, A^* = 0.6, f^* = 0.126$, at various time instants: (a) $\omega_{f,c}$, through the wake centerline FI at T1 & T3; and (b) $\omega_{f,e}$ through the exit face HI, at T1 & T3.

recovers. The reverse flow is directly proportional to the deflected profile as expected and increases with the increase in Reynolds number.

By integrating the velocity profile of the deflected flow and the reverse flow, and by taking the ratio, one can obtain the fraction of the wake fluid that is drawn into disrupting the boundary layer. The rest of the fluid disrupts the main flow into the control volume. The ratio α_b at an instant is defined as, $\alpha_b = \int_{y_c}^{y_p} u dy / \int_{x_c}^{x_o} v dx$, and is calculated numerically. The x_o is the nearest location to the bluff body at which the transverse velocity profile through plane CN changes its sign and y_p is the point at which axial velocity through the inlet face CG changes its sign. The above defined limits of the integration vary for different Re, to meaningfully represent the regions of total deflected flow from the wake and the reverse flow which penetrate into the boundary layer. The ratio is plotted for different Re in Fig. 13(d) for the time instant T1. The fraction of the fluid that enters the boundary layer varies from 0.35 to 0.45, while rest of the flow severs the supply of circulation to further downstream. For low Reynolds number, the fraction of fluid that penetrated increases,

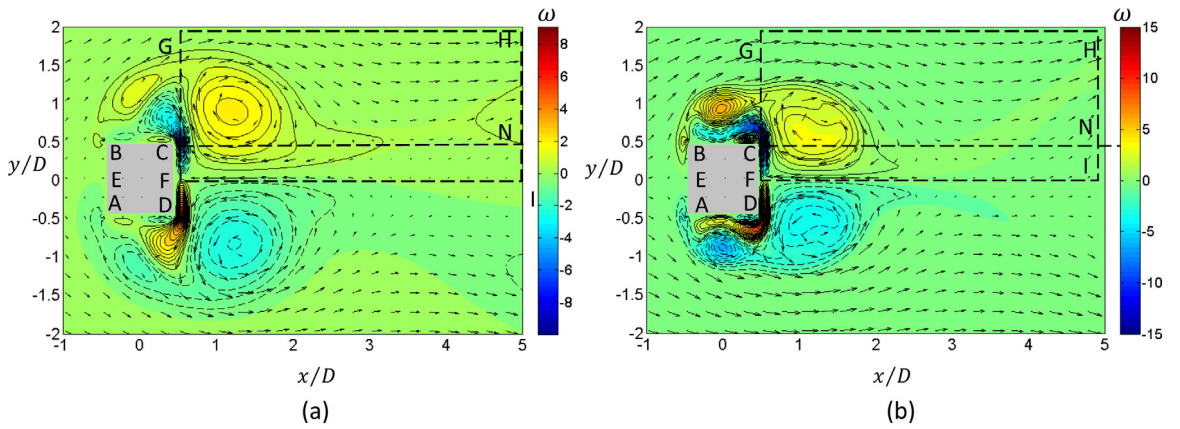

Fig. 12. Vorticity contours and superimposed velocity vectors shown at the instant T1 for: (a) Re = 50 (top); (b) Re = 100 (bottom). Here, $A^* = 0.6$ and $f^* = 0.126$.

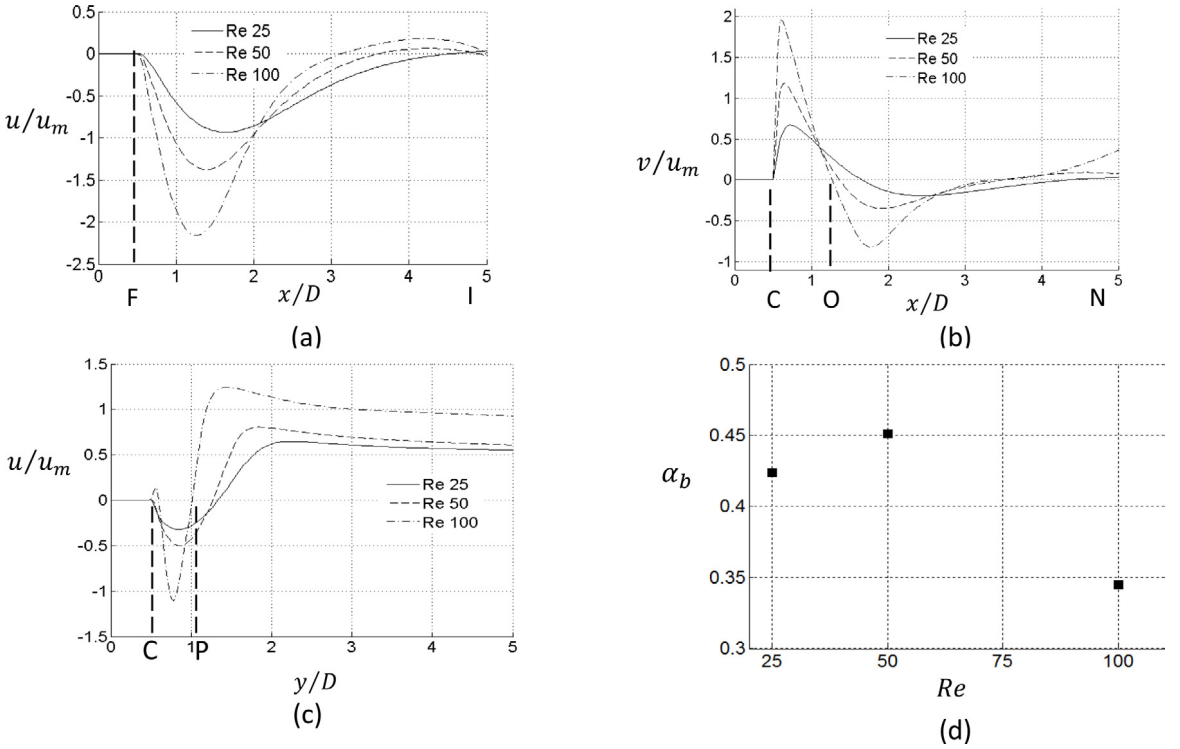

Fig. 13. Velocity plots at T1 for various Reynolds numbers, for fixed $A^* = 0.6$ and $f^* = 0.126$. (a) Wake centerline velocity, (b) transverse velocity component though plane CN, (c) boundary-layer reverse flow though face CG, and (d) flow ratio, α_b, at instant T1.

probably due to the lower momentum of the boundary layer compared to the situation at high Reynolds numbers. The vorticity transport into the control volume is similar for all Reynolds numbers examined.

Positive vorticity is convected into the control volume and undergoes diffusion and annihilation with counter-current-flow produced negative vorticity, and with negative shear-layer vorticity generated at the front and side walls. generated at the front and side walls. The surviving vorticity after this annihilation is convected out of the control volume. The surviving negative base-region vorticity within the control volume is transported upstream by the strong counter-current flow and undergoes considerable annihilation outside of the control volume. A small amount of the negative base region vorticity generated is lost to the adjacent positive base-region vorticity in addition to the main shear layer interaction.

By carrying out an analysis of vorticity transport for a control volume FGHI located in the wake, the interaction of different vortical regions and processes can be quantified. The net vorticity flux with positive vorticity, which enter control volume FGHI through face FG at an instant, $\omega_{tp} = \int_{y_C}^{y_G} (\omega_{f,c} + \omega_{f,d})\, dy$, is evaluated numerically in a similar manner to

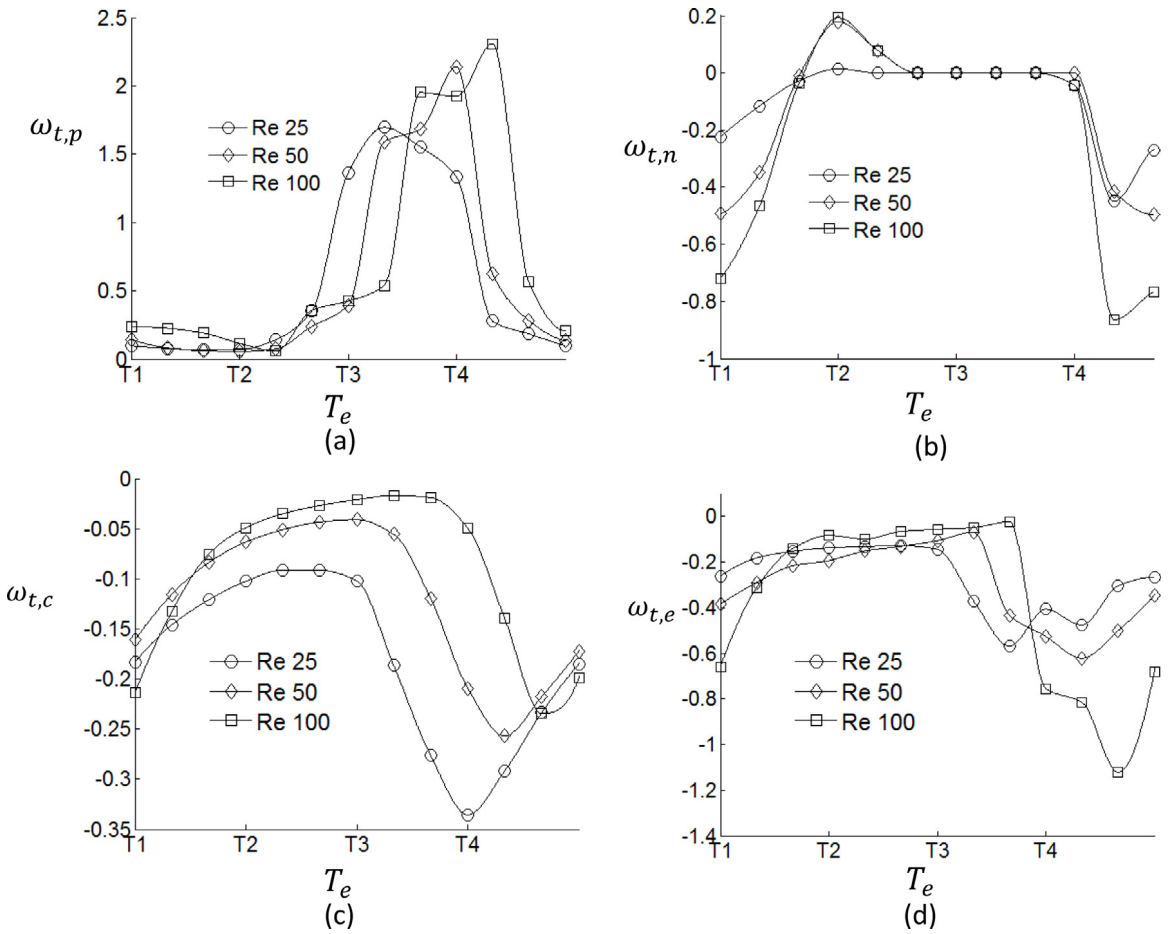

Fig. 14. Spatially integrated unsteady vorticity flux through the control volume boundaries at various instants for various Reynolds numbers. (a) $\omega_{t,p}$, (positive vorticity) through the face CG, (b) $\omega_{t,n}$, (negative vorticity) through face CG, (c) $\omega_{t,c}$ (positive vorticity) through the wake centerline FI, and (d) $\omega_{t,e}$ (positive vorticity) through the exit face HI. The y-ordinate scale change in each subfigure.

the steady inflow case and is shown in Fig. 14(a) for different Reynolds numbers, for $A^* = 0.6$ and $f^* = 0.126$. It can be observed that the net transport of vorticity is highly unsteady, with most of the vorticity transported into the wake over the latter part of the cycle. As the Reynolds number is increased, the vorticity transport into the wake increases. Through face FG there is also transport of the negative vorticity by part of the wake counter flow that penetrates into the boundary layer. The net flux of the spatially integrated negative vorticity profile at each instant, denoted as ω_{tn} is also evaluated similar to ω_{tp} and plotted in Fig. 14(b). As the Reynolds number is increased, there is increased transport of negative vorticity upstream. There is also a small amount of positive gain of negative vorticity through the control volume face when some of the vorticity is again down-washed into the control volume. However, overall, a considerable amount of vorticity is annihilated upstream. In Fig. 14(c) & (d), the net positive vorticity that is annihilated across the centerline FI, $\omega_{t,c}$ and the net positive vorticity that is convected out through the face HI $\omega_{t,c}$ are shown respectively. As the Reynolds number is increased, the diffusive flux between shear layers decreases, while the interaction between the base region vorticity and the shear layer vorticity increases. This is because the fraction of the deflected flow causes the shear layers to be pushed apart. Further downstream towards the exit these oppositely vortical regions cancel each other.

By once again integrating the spatially integrated vorticity flux over time, the net positive circulation that is transported into the control volume can be obtained by evaluating $\Gamma_{tot,p} = \int_0^{T_e} \omega_{tp}\, dt$ numerically. Similarly, the circulation that is annihilated at the centerline $\Gamma_c = \int_0^{T_e} \omega_{tc}\, dt$ and circulation that escapes through the exit face $\Gamma_e = \int_0^{T_e} \omega_{te}\, dt$ over a cycle is calculated. The fraction of vorticity annihilated on the centerline $\alpha_{dc} = \Gamma_c/\Gamma_{tot,p}$, that convected out through exit face $\alpha_{ce} = \Gamma_e/\Gamma_{tot,p}$ and that destroyed at the base region vorticity interface within control volume $\alpha_i = [1 - (\alpha_{dc} + \alpha_{ce})]$, were each computed and given in Fig. 15 in the form of bar graph.

The counter-current flow observed is present at lower amplitudes as well, however, the magnitude of the counter-current flow is lower, and therefore both the disruption of the boundary layer and the induced generation of the base region vorticity are much lower. In the symmetric vortex shedding mode, the shear-layer instability is completely

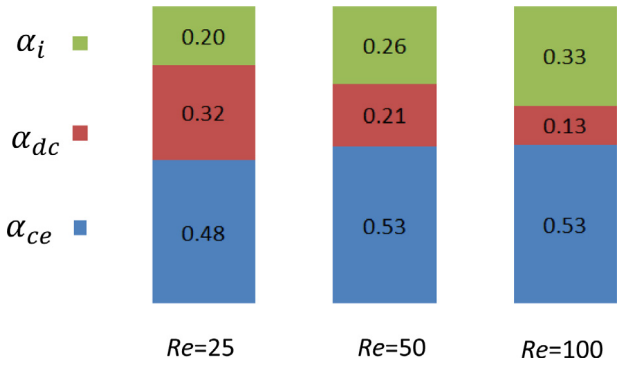

Fig. 15. Vorticity budget for the transport through the control volume FGHI, for varying Re, fixed $A^* = 0.6$ and $f^* = 0.126$. For the definition of α_i, α_{dc}, α_{ce} refer text.

Table 2
Vorticity generation and transport for symmetric mode, Literature summary.

Author	Vorticity production	Vorticity transport
Xu et al. (2006),	Relatively steady pressure gradient pressure generation is assumed.	Does not account for the vorticity transport in the wake.
Al-Mdallal et al. (2007)	Attributes base region vorticity to entrapped shear layer vorticity	Does not account for the vorticity transport in the wake.
Srikanth et al. (2011)	Base region vorticity production is attributed to a *ground* effect	Does not account for the vorticity transport in the wake.
Naudascher	Does not account for change in vorticity production on the surface.	Identifies the strongly periodic wake counter current flow and is attributed to relative motion between bluff body and fluid.

suppressed. However, at lower amplitudes, the counter-current flow interacts with the shear-layer instability above the critical Reynolds number and gives rise to different forced vortex shedding modes. Fig. 16(a), shows a snapshot of vorticity and velocity contours for $Re = 25, A^* = 0.4$ and $f^* = 0.126$. The vorticity dynamics are similar to the $Re = 25, A^* = 0.6$ and $f^* = 0.126$ case, except that, due to the relatively lower strength of the counter-current flow boundary layer, penetration of the flow is minimal. The small amount of base region vorticity interacts with the main shear layer periodically, giving rise to the wavy appearance of the vorticity contour profile. In Fig. 16(b), a snapshot of vorticity and velocity contours for $Re = 50, A^* = 0.4$ and $f^* = 0.126$ is shown. The entrainment analysis of these forced vortex shedding modes is considerably more involved due to the moving interface between shear layers and non-negligible contribution of base region vorticity to the overall vorticity dynamics. The entrainment analysis other forced vortex shedding modes will be addressed in a future work.

One interesting phenomenon observed is that the near-body wake is dominated by the counter-current flow. However, the counter-current flow is not completely symmetric and the shear-layer instability is not completely suppressed. At the tail end of the shear layers the instability sets in, and further downstream the vortices arrange in an antisymmetric pattern. In Fig. 17, snapshots of vorticity and velocity contours for $Re = 100, A^* = 0.4$ and $f^* = 0.126$ are shown at time instants T1 and T3. It is noticeable that at the start of the cycle there is a strong flow towards the base region at an angle to the wake axis. This strongly drawn fluid considerably disrupts the vorticity transport, and both vortices tend to form together, and the entrainment mechanism is almost suppressed over the first half of the cycle. During the second half of the cycle, weak entrainment leads to the shedding of both pairs into the wake.

6. Discussion

For the natural vortex shedding mode, the relatively steady generation of vorticity at the bluff body walls and the subsequent transport into the wake, together with strong redistribution due to the entrainment mechanism in the near wake, provides a description of wake vorticity dynamics from a two-dimensional perspective. A similar attempt to understand the vorticity dynamics under excited conditions must take into account the alteration to boundary vorticity flux as well as the alteration to the nature of transport of vorticity due to excitation. In Table 2, a summary of various accounts in literature on the nature of vorticity generation and transport under symmetric vortex shedding is given. While a few authors have commented on the nature of vorticity production, a control volume analysis of vorticity transport such as presented in the present work is absent in literature.

By varying the Reynolds number for fixed amplitude and frequency ratio one can decouple the effects of relative-velocity-based pressure-gradient vorticity generation and wall-vorticity-based pressure-gradient vorticity generation. If

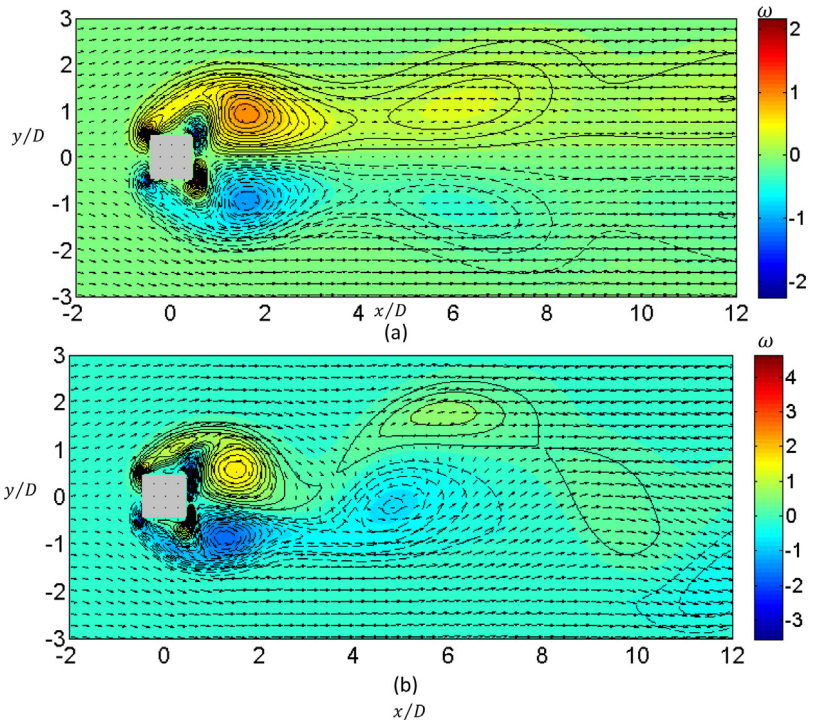

Fig. 16. Vorticity contours and superimposed, velocity vectors shown at the instant T1 for (a) $Re = 25$ and (b) $Re = 50$, for fixed $A^* = 0.4$ and $f^* = 0.126$.

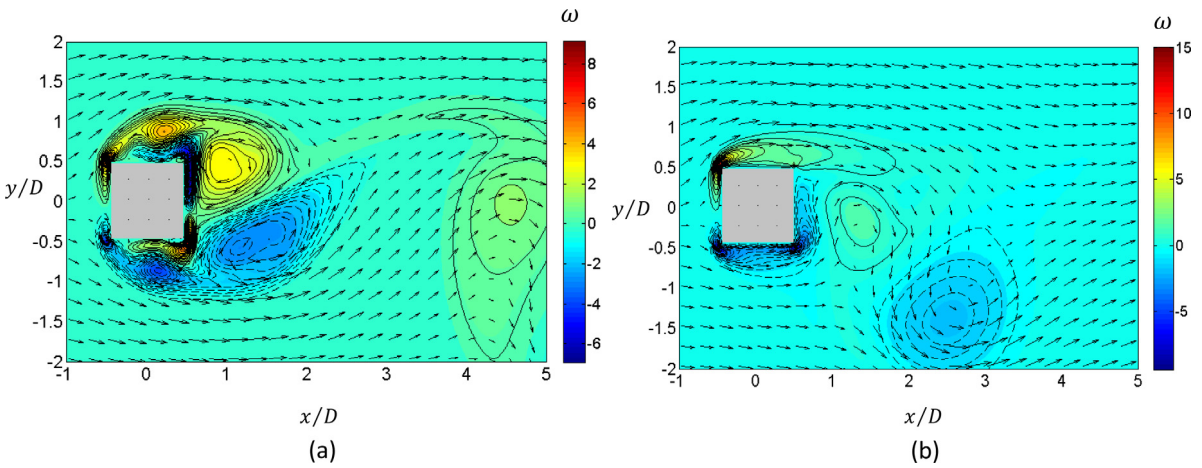

Fig. 17. Vorticity contours and velocity vectors shown for $Re = 100$, $A^* = 0.4$ and $f^* = 0.126$ for P mode formation: (a) at time T1; (b) at time T3.

the picture presented by Xu et al. (2006) that major source of unsteady vorticity is due to the boundary acceleration holds true, then lowering the Reynolds number while keeping the amplitude ratio and frequency ratio constant will cause the symmetric vortex shedding to be more intense at lower Reynolds numbers, since the constant pressure-gradient-based generation reduces with Reynolds number and the acceleration-based vorticity generation will dominate the vorticity dynamics. If the strong wall-vorticity-interaction-based pressure-gradient generation holds true then it should be deemed that a stronger circulation region, forming closer to the body, will accelerate more fluid towards the base wall. Partly the difficulty in discerning the different causes of vorticity production at boundary surfaces is that all terms are correlated to an extent with the fluctuating velocity.

In Fig. 18, various parameters in the near wake that characterize the strength of symmetric vortex shedding, such as the nondimensionalized strength of the circulation within the control volume FGHI at the instant T1 denoted as $\Gamma_{w,max}$, vorticity maxima in the near wake denoted as $\omega_{w,max}$, the distance of vorticity maxima from the center of the square

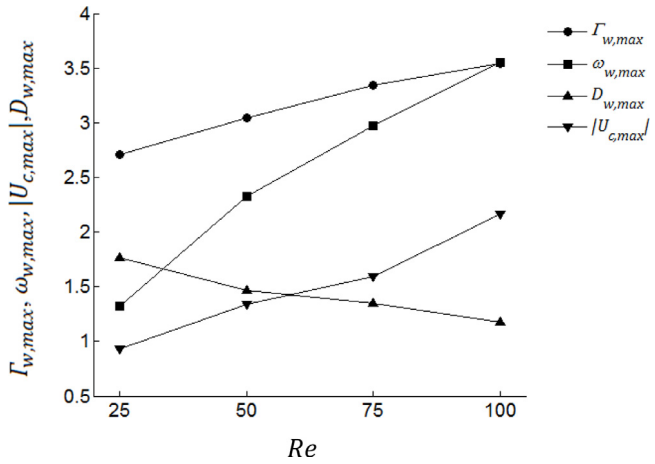

Fig. 18. Symmetric mode intensity comparison for different Reynolds numbers for $A^* = 0.6$ and $f^* = 0.126$. For the description of various quantities plotted refer text. On the ordinate axis all the quantities are nondimensionalized.

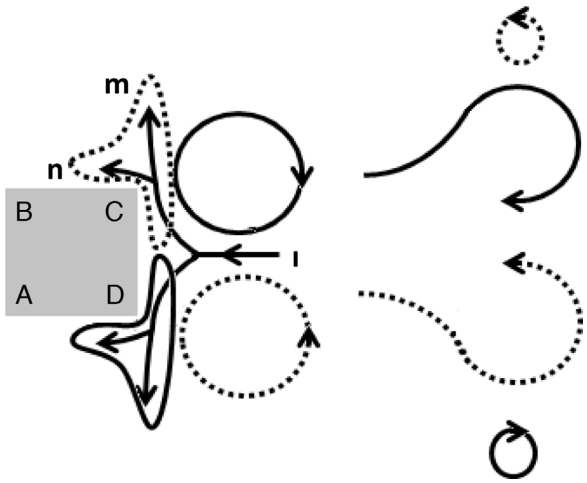

Fig. 19. Mechanism of symmetric mode formation.

cylinder denoted as $D_{w,max}$ and absolute value of maximum magnitude of wake counter flow denoted as $|U_{c,max}|$, are plotted. From Fig. 18, it can be observed that parameters $\Gamma_{w,max}$, $\omega_{w,max}$ and $|U_{c,max}|$ increase with Reynolds number. The increase in wake counter flow is remarkable in that it acts like an inverse jet in the wake. Naudascher attributes wake counter flow to the relative motion between bluff body and wake fluid. However, the relative motion of the bluff body and mean flow, alone cannot account for the jet-like nature of the wake counter flow, which exceeds the magnitude of bluff body and mean flow velocity, combined. As the Reynolds number increases, $D_{w,max}$ decreases which imply that the maximum wake counter-flow velocity is strongly correlated with the stronger circulation region forming closer to the wall. As the Reynolds number is increased more vorticity is transported into the wake, which also means that the strength of the vorticity the rolls up nearer to the wall also increases, this in turn accelerates more fluid towards the base region.

The mechanism of symmetric vortex shedding can be understood with the diagram shown in Fig. 19. During the part of the cycle when there is vorticity generation close to the rear wall, fluid is accelerated towards the base region and a considerable amount of vorticity, opposite in sign to the adjacent main shear layer, is generated especially around the rear sharp corners. The strong wake counter flow shown as 'l' in Fig. 19, encounters the base region wall and effectively splits into two branches. The fluid branch, shown as 'n' in Fig. 19, disrupts the low velocity boundary-layer flow while another part shown as 'm', cuts through the main separating shear layer. Considerable vorticity annihilation with the main shear layer is caused by both branches as both fluid branches carry opposite-signed vorticity. The base region vorticity gradually weakens due to vorticity annihilation by branches 'm' and 'n', as well as through the convection of shear layer vorticity away from the wall by fluid branch 'm'. The main flow also recovers near the boundary layer during this time. If some of the vorticity carried by fluid branch 'm' survives the annihilation process, two counter-rotating vortex pairs are formed

resulting in the S-II mode, otherwise the usual symmetric vortex pair mode forms. The trail of the branch of fluid that penetrates through the shear layer carrying negative vorticity is a very visible feature in both the experimental results of Ongoren and Rockwell (1988) and numerical results of Al-Mdallal et al. (2007). The closer formation of vortices and the narrowing of the wake as described by Naudascher (1987) is due to the inviscid flow towards the wake centerline to replenish fluid in the wake. At lower amplitudes, the wake fluid does not have enough momentum to achieve this. However, it can interact with fluid shown as branch 'b' in Gerrard's mechanism, thereby altering the entrainment process and resulting in different modes.

The above mechanism can explain a few observations about the symmetric mode appearing in the literature. While usually symmetric vortex shedding can be expected to occur at higher amplitudes and higher frequencies, a number of authors have reported that symmetric vortex shedding occurs at the left lock-in boundary of the fundamental synchronization region, at lower amplitudes. A good question to ask is why symmetric vortex shedding, which implies imposition of an external frequency, appears at the left lock-in region at relatively lower amplitudes (Barbi et al., 1986; Konstantinidis and Balabani, 2007). Within the synchronization region, the influence of the external forcing is maximum, and if one were to hypothesize that the time scale for the interaction of the vortex with the rear wall is important, then one should expect that the maximum time for interaction will occur at the left lock-in boundary. This may explain the occurrence of symmetric vortex shedding at the left lock-in boundary. The above mechanism can also explain why the response of different bluff bodies may be different around the fundamental synchronization region. For a circular cylinder, it can be expected that the wake counter flow will be more smoothly interrupted by the rear wall, while the ratio of the boundary-layer-disrupting flow to the flow cutting the shear layer can be different. Since for square cylinders most of the vorticity generation occurs at the front sharp corners, the boundary-layer disruption may not be as significant compared to a circular cylinder for given amplitude. The boundary layer disrupting flow implies that at the surface there is a competition between both the counter-flow branch and the main flow, for vorticity production. Any vorticity production area that is lost to the main flow is a gain for the counter flow and vice versa. Whether such competition is responsible for the reduction in the natural vortex shedding frequency observed by Leontini et al. (2011) and Smith et al. (2012) around the subharmonic synchronization boundaries needs to be further investigated in future work.

7. Summary and conclusions

In the present study, we characterize the strong unsteady vorticity production and transport in the flow past a square cylinder subjected to inline pulsatile flow, under symmetric vortex shedding. By using a square cylinder and through considering the equivalency of this problem with inline vibration of a square cylinder under mean flow, it was expected that a strong unsteady and spatially uniform vorticity profile will be observed at the top and bottom walls, due to the equivalent acceleration-based vorticity generation. However, the results presented indicate that unsteady non-uniform vorticity production around the front and rear sharp corners is significant, indicating strong unsteady vorticity generation due to an altered tangential pressure gradient around the bluff body. It is observed that the unsteady base region vorticity, which is opposite in sign to that of the adjacent main shear layer, is directly proportional to the strong wake counter flow. The wake counter flow branches into two parts, with one disrupting the boundary layer flow while other cuts off the supply of circulation to the shear layer, while carrying the base region vorticity. If the wake counter flow has enough momentum, then the base region vorticity can form a pair with the shear-layer vorticity to result in a symmetric vortex pair shedding mode. Thus the strong wake counter flow is an essential feature of symmetric vortex shedding.

In order to further understand the nature of pressure-gradient-based vorticity generation, wake counter flow and the role of base region vorticity in the vorticity dynamics, the Reynolds number based on the mean flow was varied while keeping the amplitude ratio and the frequency ratio based on the Strouhal number at $Re = 100$, constant. Contrary to the expectation that symmetric mode features will strengthen or remain constant at lower Reynolds number, it is observed that symmetric flow features increase with the Reynolds number. This is indicated by the stronger wake counter flow and increased annihilation between base region vorticity and the main shear layer at the higher Reynolds numbers considered in the present study. The strong wake counter flow cannot be attributed to the relative flow between mean flow and fluctuating flow alone either, since the magnitude of wake counter flow is rather jet-like in its nature. It is concluded that the strong wall vortex interaction between the rolled-up shear layer and base region wall contributes significantly to the wake counter flow and associated base region vorticity generation. At lower amplitudes, the wake counter flow can interact with the cross-wake entrainment flow to result in different vortex shedding modes, if the natural vortex shedding is present at a particular Reynolds number. Considering that the mechanism of symmetric vortex shedding and Gerrard's mechanism for natural vortex shedding are dominantly two-dimensional, competition of both mechanisms is also two-dimensional in nature.

References

Abernathy, F.H., Kronauer, R.E., 1962. The formation of vortex streets. J. Fluid Mech. 13, 1–20.
Agrawal, A., Agrawal, A., 2006. Three-dimensional simulation of gaseous slip flow in different aspect ratio microducts. Phys. Fluids 18, 10364.
Al-Mdallal, Q.M., Lawrence, K.P., Kocabiyik, S., 2007. Forced streamwise oscillations of a circular cylinder: Locked-on modes and resulting fluid forces. J. Fluids Struct. 23, 681–701.
Barbi, C., Favier, D.P., Maresca, C.A., Telionis, D.P., 1986. Vortex shedding and lock-on of a circular cylinder in oscillatory flow. J. Fluid Mech. 170, 527–544.

Bearman, P.W., 1984. Vortex shedding from oscillating bluff bodies. Annu. Rev. Fluid Mech. 16, 195–222.
Bearman, P.W., Downie, M.J., Graham, M.R., Obasaju, E.D., 1985. Forces on cylinders in viscous oscillatory flow at low Keulegan–Carpenter numbers. J. Fluid Mech. 154, 337–356.
Blackburn, H.M., Henderson, R., 1999. A study of two-dimensional flow past an oscillating cylinder. J. Fluid Mech. 385, 255–286.
Chen, S., Doolen, D.G., 1998. Lattice Boltzmann method for fluid flows. Annu. Rev. Fluid Mech. 30, 329–364.
Cheng, M., Lou, J., Luo, L.-S., 2010. Numerical study of a vortex ring impacting a flat wall. J. Fluid Mech. 660, 430–455.
Couder, Y., Basdevant, C., 1986. Experimental and numerical study of vortex couples in two-dimensional flows. J. Fluid Mech. 173, 225.
Detemple-Laake, E., Eckelmann, H., 1989. Phenomenology of Karman vortex streets in oscillatory flow. Exp. Fluids 7, 217–227.
Franke, R., Rodi, W., Schonugh, B., 1990. Numerical calculation of laminar vortex-shedding flow past cylinders. J. Wind Eng. Ind. Aerodyn. 35, 237–257.
Gerrard, J.H., 1966. The mechanics of the formation region of vortices behind bluff bodies. J. Fluid Mech. 401–413, 25.
Griffin, O.M., Hall, M.S., 1991. Review-vortex shedding lock-on and flow control in bluff body wakes. J. Fluids Eng. 113, 526–537.
Konstantinidis, E., Balabani, S., 2007. Symmetric vortex shedding in the near wake of a circular cylinder due to stream wise perturbations. J. Fluids Struct. 23, 1047–1063.
Krishnan, H., Agrawal, A., Sharma, A., Sheridan, J., 2016. Near-body vorticity dynamics of a square cylinder subjected to an inline pulsatile free stream flow. Phys. Fluids 28, 093605.
Krishnan, H., Agrawal, A., Sharma, A., Thompson, M., Sheridan, J., 2018. Characteristics of force coefficients and energy transfer for vortex shedding modes of a square cylinder subjected to inline excitation. J. Fluids Struct. 81, 270–288.
Kumar, S.R., Sharma, A., Agrawal, A., 2008. Simulation of flow around a row of square cylinders. J. Fluid Mech. 606, 369–397.
Leontini, J.S., Jacono, D.L., Thompson, M.C., 2011. A numerical study of an inline oscillating cylinder in a free stream. J. Fluid Mech. 688, 551–568.
Morton, B.R., 1984. Generation and decay of vorticity. Geophys. Astrophys. Fluid Dyn. 28, 277–308.
Naguib, A.M., Koochesfahani, M.M., 2004. On wall-pressure sources associated with the unsteady separation in a vortex-ring/wall interaction. Phys. Fluids 16 (7), 2613–2622.
Naudascher, E., 1987. Flow-induced streamwise vibrations of structures. J. Fluids Struct. 1, 265–298.
Ongoren, A., Rockwell, D., 1988. Flow structure from an oscillating cylinder part 2. mode competition in the near wake. J. Fluid Mech. 191, 225–245.
Perdikaris, P.G., Kaitsis, L., Triantafyllou, G.S., 2009. Chaos in a cylinder wake due to forcing at the strouhal frequency. Phys. Fluids 21.
Robichaux, J., Balachandar, S., Vanka, S.P., 1999. Two-dimensional Floquet instability of the wake of square cylinder. Phys. Fluids 11, 560–578.
Roshko, A., 1954. On the development of turbulent wakes from vortex streets.
Scolan, Y.M., Faltinsen, O.M., 1994. Numerical studies of separated flow from bodies with sharp corners by the vortex in cell method. J. Fluids Struct. 8, 201–230.
Sewatkar, C.M., Sharma, A., Agrawal, A., 2011. Simulation of flow across a row of transversely oscillating square cylinders. J. Fluid Mech. 680, 361–397.
Sharma, A., Eswaran, V., 2004. Heat and fluid flow across a square cylinder in the two-dimensional laminar flow regime. Numer. Heat Transfer A 45, 247–269.
Smith, D.T., Leontini, J.S., Sheridan, J., Lo Jacono, D., 2012. Streamwise forced oscillations of circular and square cylinders. Phys. Fluids 24, 111703.
Sohankar, A., Norberg, C., Davidson, L., 1997. Numerical simulation of unsteady low-Reynolds number flow around rectangular cylinders at incidence. J. Wind Eng. Ind. Aerodyn. 69–71, 189–201.
Srikanth, T., Dixit, H.N., Rao, T., Govindarajan, R., 2011. Vortex shedding patterns, their competition, and chaos in flow past inline oscillating rectangular cylinders. Phys. Fluids 23, 073603.
Succi, S., 2001. The Lattice Boltzmann Equation for Fluid Dynamics and beyond. Oxford U.P.
Tanida, Y., Okajima, A., Watanabe, Y., 1973. Stability of a circular cylinder oscillating in uniform flow or in a wake. J. Fluid Mech. 61 (4), 769–784.
Williamson, C.H.K., Govardhan, R., 2004. Vortex-induced vibrations. Annu. Rev. Fluid Mech. 36, 413–455.
Williamson, C.H.K., Roshko, A., 1988. Vortex formation in the wake of an oscillating cylinder. J. Fluids Struct. 2, 355–381.
Wu, J.Z., Wu, J.M., 2006. Interactions between a solid surface and a viscous compressible flow field. J. Fluid Mech. 254, 183–211.
Xu, S.J., Zhou, Y., Wang, M.H., 2006. A symmetric binary-vortex street behind a longitudinally oscillating cylinder. J. Fluid Mech. 556, 27.